ARL-TR-7687 ● MAY 2016

US Army Research Laboratory

Incorporation and Effects of Nanoparticles in a Supramolecular Polymer

by Alice M Savage, Robert H Lambeth, and Frederick L Beyer

NOTICES

Disclaimers

The findings in this report are not to be construed as an official Department of the Army position unless so designated by other authorized documents.

Citation of manufacturer's or trade names does not constitute an official endorsement or approval of the use thereof.

Destroy this report when it is no longer needed. Do not return it to the originator.

ARL-TR-7687 ● MAY 2016

US Army Research Laboratory

Incorporation and Effects of Nanoparticles in a Supramolecular Polymer

by Alice M Savage
Oak Ridge Institute of Science and Education, Oak Ridge, TN

Robert H Lambeth and Frederick L Beyer
Weapons and Materials Research Directorate, ARL

REPORT DOCUMENTATION PAGE

Form Approved
OMB No. 0704-0188

1. REPORT DATE *(DD-MM-YYYY)*	2. REPORT TYPE	3. DATES COVERED (From - To)
May 2016	Final	October 2014–September 2015

4. TITLE AND SUBTITLE
Incorporation and Effects of Nanoparticles in a Supramolecular Polymer

5a. CONTRACT NUMBER

5b. GRANT NUMBER

5c. PROGRAM ELEMENT NUMBER

6. AUTHOR(S)
Alice M Savage, Robert H Lambeth, and Frederick L Beyer

5d. PROJECT NUMBER

5e. TASK NUMBER

5f. WORK UNIT NUMBER

7. PERFORMING ORGANIZATION NAME(S) AND ADDRESS(ES)
US Army Research Laboratory
ATTN: RDRL-WMM-G
Aberdeen Proving Ground, MD 21005-5069

8. PERFORMING ORGANIZATION REPORT NUMBER
ARL-TR-7687

9. SPONSORING/MONITORING AGENCY NAME(S) AND ADDRESS(ES)

10. SPONSOR/MONITOR'S ACRONYM(S)

11. SPONSOR/MONITOR'S REPORT NUMBER(S)

12. DISTRIBUTION/AVAILABILITY STATEMENT
Approved for public release; distribution is unlimited.

13. SUPPLEMENTARY NOTES

14. ABSTRACT
Supramolecular polymers provide potential innovative applications in coatings, adhesives, fuel cells, and biosensors due to retention of physical and mechanical properties with increased processability, self-healing, and stimuli responsiveness. Incorporating a nanoscale filler into the supramolecular polymer can improve the physical and mechanical properties and application window while still maintaining processability and stimuli responsiveness. This project primarily focuses on the design, synthesis, and morphological characterization of a series of supramolecular nanocomposite films with unfunctionalized and functionalized gold nanoparticles. Morphological effects of different nanoparticle loadings are investigated using small-angle X-ray scattering and transmission electron microscopy.

15. SUBJECT TERMS
supramolecular, assembly, metallopolymer, morphology, nanoparticles

16. SECURITY CLASSIFICATION OF:			17. LIMITATION OF ABSTRACT	18. NUMBER OF PAGES	19a. NAME OF RESPONSIBLE PERSON
a. REPORT	b. ABSTRACT	c. THIS PAGE			Alice M Savage
Unclassified	Unclassified	Unclassified	UU	28	19b. TELEPHONE NUMBER (Include area code) 410-306-0893

Standard Form 298 (Rev. 8/98)
Prescribed by ANSI Std. Z39.18

Contents

List of Figures

Acknowledgments

Alice M Savage was supported by the Postgraduate Research Participation Program at the US Army Research Laboratory, administered by the Oak Ridge Institute of Science and Education (ORISE) through an interagency agreement between the US Department of Energy and Army Research Laboratory (Contract No. ORISE 1120-1120-99).

INTENTIONALLY LEFT BLANK.

1. Introduction

Adding an inorganic or organic filler to a polymer matrix to make polymer composite materials has become a very expansive field. Interest in polymer nanocomposites increased in recent decades due to the unique characteristics of polymer modified with nanoscale-size fillers.[1] By definition, a nanocomposite comprises 2 or more dimensions (phases) where one or more of the filler dimensions is of nanometer or 10s of nanometers scale.[2,3] The increased optical, mechanical, chemical, electrical, and reinforcement properties of the nanocomposites arising from the size-dependent properties of the nanoscale filler afford diverse applications in protection, cosmetics, automobiles, sporting goods, electronics, etc.[3]

More recently, functionalized nanoparticles in composites have been found to affect the bulk polymer morphology by manipulating the miscibility between the nanoscale filler and the polymer matrix.[4–6] The particles can participate in the polymer matrix and affect the phase diagram, resulting in a change in polymer morphology, increased structural control, and, potentially, improved mechanical properties.[7] To make stimuli-responsive composites, supramolecular polymers matrices were used to afford well-controlled nanostructures.[3,8–12]

Supramolecular polymers,[13] defined as polymers formed by assembly of one or more molecular components with reversible bonds and large association constants ($Ka \approx 10^6$ to 10^{21}), offer good materials properties with better processability and a stimuli-responsive behavior.[13–17] The Rowan and Weder groups developed an optically healable supramolecular polymer system that uses the strong metal-coordination bonds of a divalent (or trivalent) metal cation to a pyridine-based ligand 2,6-bis(1'-methyl-benzimidazolyl)-4-hydroxypyridine (MeBIP).[18–24] Supramolecular polymers of a telechelic macromonomer (BKB, poly(ethylene-*co*-butylene) polymer core, and MeBIP endcaps) and a Zn^{2+} or La^{2+} salt formed optically healable free-standing films. These elastomeric films microphase separate into metal-ligand complex-rich domains and polymer core domains similar to those formed by polyurethane hard and soft segments.[18,20] However, these films lack the toughness and stiffness needed for many US Army applications. One method to improve the physical properties of a film is to alter the morphology of the polymer matrix.[25]

Supramolecular polymers provide potential innovative applications in coatings, adhesives, fuel cells, and biosensors due to retention of physical and mechanical properties with increased processability, self-healing, and stimuli responsiveness. Incorporating a nanoscale filler into the supramolecular polymer can improve the

physical and mechanical properties and application window while still maintaining processability and stimuli responsiveness. This project primarily focuses on the design, synthesis, and morphological characterization of a series of supramolecular nanocomposite films with unfunctionalized and functionalized gold (Au) nanoparticles. Morphological effects of different nanoparticle loadings are investigated using small-angle X-ray scattering (SAXS) and transmission electron microscopy (TEM).

To modify the morphology of BKB supramolecular polymer films, we synthesized supramolecular nanocomposites comprising Au nanoparticles functionalized with MeBIP ligands (MeBIP-gold nanoparticles [AuNps]) that directly influence the supramolecular polymer formation (Fig. 1). The morphological effects of nanoparticle loadings (0–1.5 wt%) within the BKB supramolecular polymer were investigated using SAXS and TEM.

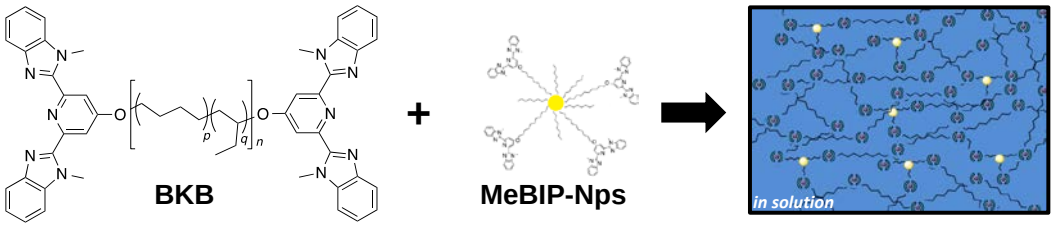

Fig. 1 Supramolecular polymer nanocomposite components

2. Experimental

2.1 Materials

Shown in Fig. 2, 2,6-bis(1'-methyl-benzimidazolyl)-4-hydroxypyridine (MeBIP-OH) was synthesized as reported.[19] BKB macromonomer was also synthesized as reported.[18] Potassium hydroxide (KOH, Aldrich, 85.0%), 1,2-dibromododecane (Aldrich, 98%), dimethyl sulfoxide (DMSO, anhydrous, Aldrich, 99%), potassium thioacetate (Aldrich, 98%), *N*,*N*-dimethylformamide (DMF, Aldrich, 99.8%), chloroform ($CHCl_3$, Aldrich), magnesium sulfate (Aldrich, 97%), methanol (MeOH, Aldrich), hydrochloric acid (HCl, Fisher Scientific), zinc (II) perchlorate hexahydrate ($Zn(ClO_4)_2$, Aldrich), 1-octanethiol (OCT, Aldrich, 98.5%), didodecyldimethylammonium bromide (DDAB, Aldrich, 98%), Au (III) chloride ($AuCl_3$, Aldrich, 99%), borane tert-butylamine complex (TBAB, Aldrich, 97%), phosphoric acid (Fischer Scientific), triphenylphosphine (Aldrich, 99%), diethyl azodicarboxylate (40 wt% in toluene) and acetonitrile (ACN, Aldrich, 99.8%) were used as received.

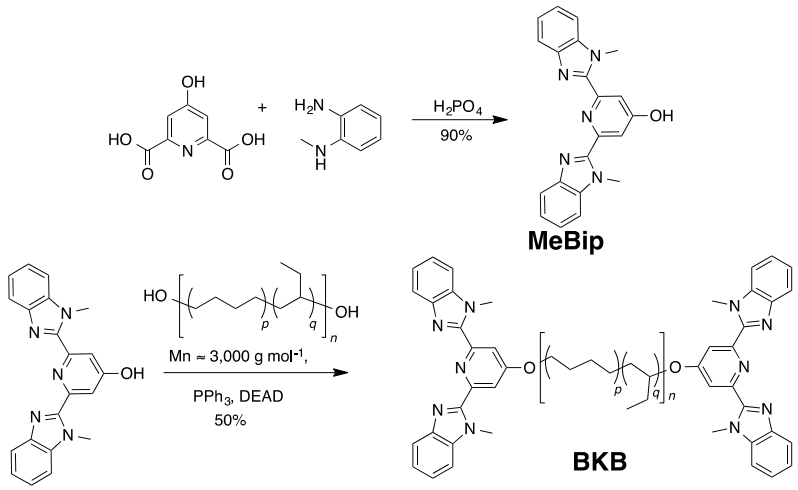

Fig. 2 Synthesis of MeBIP-OH[19] and BKB macromonomer[18,22]

2.2 Instrumentation

TEM was performed on samples prepared using a Leica FC7 ultramicrotome equipped with a Leica UC7 cryostage, with which sections approximately 50 nm in thickness were cut using a Diatome diamond knife at –80 °C. High-angle annular dark field scanning TEM (HAADF STEM) was performed using a JEOL JEM-2100F TEM, and a Gatan 806 HAADF STEM detector was used to collect dark field data. The TEM was operated at 200 kV, with a 40-μm condenser aperture, a HAADF STEM collection angle of 48–168 mrad, and spot size of 0.2 nm. A Gatan Digital Micrograph was used to collect and analyze the data. In dark field images, high Z regions appear bright and low Z regions are dark. SAXS data were collected using a Rigaku S-MAXS 3000 SAXS camera. X-rays were generated using a MicroMax-007HFM rotating copper anode source and then focused and monochromated using a Confocal Max-Flux double-focusing optic. Wavelength, λ, was 1.54059 Å. Samples were characterized over a range of momentum transfer vector magnitude, q, of 0.01 $Å^{-1}$ to 0.7 $Å^{-1}$. Distance and beam center calibrations were performed with silver behenate. Type 2 glassy carbon previously calibrated at the Advance Photon Source, Argonne National Laboratory (ANL), was used as a secondary intensity standard.[26] Data processing and analysis were performed using Igor Pro 6.3 and procedures developed at ANL.[27]

Ultraviolet-visible (UV-Vis) spectra of the nanoparticles and supramolecular polymers were collected at a wavelength range of 250–900 nm in $CHCl_3$ at room temperature using a Perkin Elmer UV/VIS/NIR (near infrared) Lambda 1050 spectrophotometer with a 3D WB (triple detector, wide band) detector module.

2.3 Synthesis of 2,6-Bis(1'-Methylbenzimidazoyl)-4-(12-Thiododecyl)pyridine (MeBIP-SH)

Freshly ground and powdered KOH (0.98 g, 17.53 mmol) and dry DMSO (80 mL) were added to a 100-mL round bottom flask with a stir bar, septum, and needle under nitrogen. After the KOH dissolved, MeBIP-OH (2.5 g, 7.01 mmol) and 1,12-dibromododecane were added to the reaction flask and stirred at 35 °C overnight. The reaction mixture was poured into ice water (200 mL) and filtered. The crude product was purified by column chromatography (silica gel, $CHCl_3$) to yield 2,6-bis(1'-methylbenzimidazoyl)-4-(12-bromododecyl)pyridine, a white solid (3.0 g, 71%).

The 2,6-bis(1'-methylbenzimidazoyl)-4-(12-bromododecyl)pyridine (2.0 g, 3.30 mmol) and dry DMF (50 mL) were added to a 100-mL round bottom flask with stir bar, septum, and a needle under nitrogen and chilled in an ice bath. After 20 min, potassium thioacetate (1.1 g, 9.63 mmol) was added to the reaction mixture and stirred overnight, allowing the ice bath to warm to room temperature. The product was extracted with $CHCl_3$ (60 mL) and water (50 mL). The $CHCl_3$ fraction was concentrated in vacuo, and the white solid (2,6-bis(1'-methylbenzimidazoyl)-4-(12-methalthioatedodecyl)pyridine) was purified by recrystallization with hot hexanes. The white solid was used in the next step without further purification.

MeBIP-SH (0.45 g, 0.8 mmol) and MeOH (30 mL) were added to a 100-mL round bottom flask with condenser, septum, and a needle under nitrogen. HCl was added until the pH of the reaction mixture reached pH 2. The reaction mixture was refluxed overnight and concentrated in vacuo to yield a yellow solid (0.40 g, 83%). A synthetic scheme for the final product of MeBIP-SH is shown in Fig. 3.

Fig. 3 Synthesis of MeBIP-SH thiol ligand

2.4 Synthesis of Octanethiol-Functionalized Gold Nanoparticles (2 nm) (OCT-AuNps)

All glassware was thoroughly cleaned, rinsed with aqua regia, and dried in a vacuum oven before use. $AuCl_3$ (150 mg) and 20 mL of a 100-mM DDAB in toluene solution were added to a 50-mL round bottom flask with septum. The flask was sonicated until $AuCl_3$ dissolved and then purged with nitrogen for 20 min. In separate flasks, OCT (0.48 mL, 2.8 mmol) was dissolved in a 100-mM DDAB solution (5 mL) and TBAB (0.68 g, 7.76 mmol) was dissolved in a 100 mM DDAB solution (10 mL). The OCT/DDAB solution was quickly added to the $AuCl_3$ reaction mixture, and the solution color changed from red to yellow. After 20 min, the TBAB/DDAB solution was then quickly added to the reaction mixture, and the solution color turned from yellow to clear and then purple after 5 min. The reaction mixture was stirred for 4 h under nitrogen and then poured into 200-mL MeOH. The nanoparticles were collected and purified by centrifugation in MeOH 3 times and dried in a vacuum oven overnight.

2.5 Synthesis of MeBIP-Functionalized Gold Nanoparticles (2 nm) (MeBIP-AuNps)

All glassware was thoroughly cleaned, rinsed with aqua regia, and dried in a vacuum oven before use. In separate flasks, OCT (0.017 mL, 0.14 mmol) was dissolved in 1 mL of $CHCl_3$, TBAB (0.068 g, 0.78 mmol) was dissolved in 100-mM DDAB solution (5 mL), and MeBIP-SH (0.078 g, 0.14 mmol) was dissolved in $CHCl_3$ (2 mL). $AuCl_3$ (15 mg) and 3 mL of a 100-mM DDAB in toluene solution were added to a 25-mL round bottom flask with septum. The flask was sonicated until $AuCl_3$ dissolved and then purged with nitrogen for 20 min. The OCT solution and MeBIP-SH solution were mixed together and quickly added to the $AuCl_3$ reaction mixture, resulting in the solution color changing from red to yellow. After 20 min, the TBAB/DDAB solution was then quickly added to the reaction mixture and the solution color immediately turned from yellow to clear and then purple after 5 min. The reaction mixture was stirred for 4 h under nitrogen and then poured into 200 mL MeOH. The MeBIP-functionalized nanoparticles (Fig. 4) were collected and purified by centrifugation in MeOH 3 times. UV-Vis was used to detect free MeBIP-SH ligand in the methanol wash. After no MeBIP-SH was detected, the nanoparticles were dried in a vacuum oven overnight. A UV-Vis titration was used to measure MeBIP concentration per nanoparticle (Fig. 5).

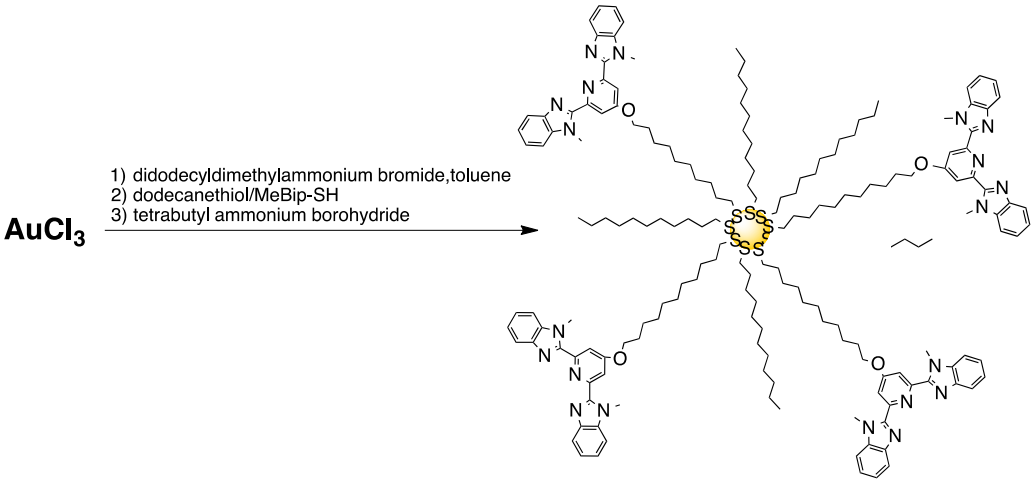

Fig. 4 Synthesis of MeBIP-AuNps-functionalized Au nanoparticles

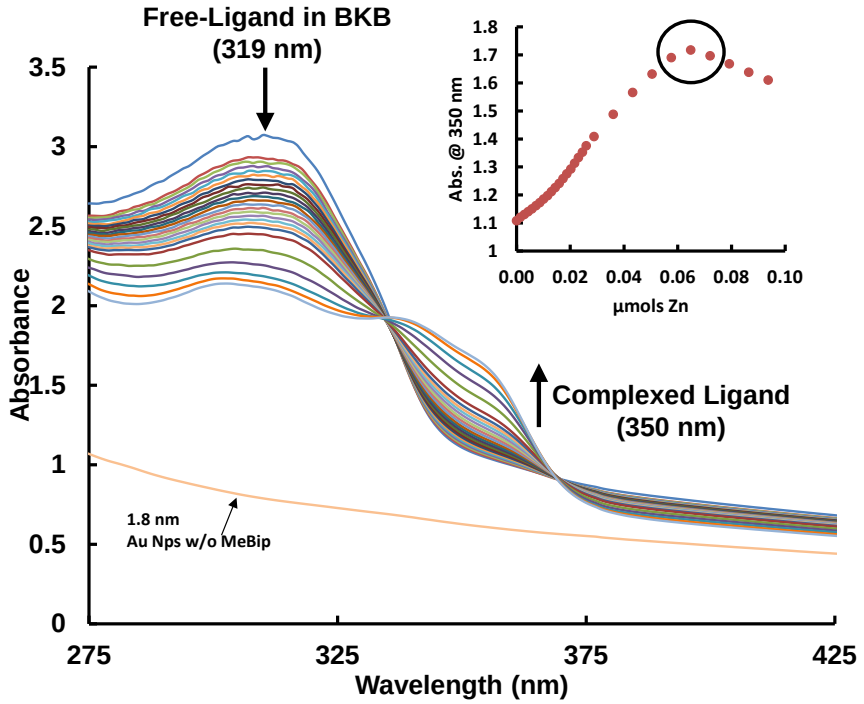

Fig. 5 Titration of MeBIP-AuNps with $Zn(ClO_4)_2$ monitored with UV-Vis. The black circle locates the isobestic point, which corresponds to the moles of MeBIP ligand per gram of MeBIP-AuNps. UV-Vis of AuNps without MeBIP-SH ligands (OCT-AuNps) is shown in yellow.

2.6 Synthesis of Metallo-Supramolecular Polymer Films

BKB (100 mg, M_n = 3,700 $gmol^{-1}$, 0.027 mmol) was dissolved in $CHCl_3$ (2.5 mL) in a 20-mL scintillation vial. $Zn(ClO_4)_2$ (10.06 mg, 0.027 mmol) was dissolved in ACN (2.5 mL) in a different 20-mL scintillation vial. OCT-AuNps or MeBIP-

AuNps (0.0–1.5 mg, 0.0001 mmol) was dissolved in $CHCl_3$ (1 mL) in another 20-mL scintillation vial. The Nps solution was added to the $Zn(ClO_4)_2$ solution and stirred for 20 min. This solution was then added to the BKB solution and stirred for 30 min. The solvent was evaporated and dried in a vacuum oven overnight. The solids were redissolved in $CHCl_3$ (1 mL) and cast in a Teflon mold. After 6 h the films were dried in a vacuum oven overnight at 40 °C.

3. Results and Discussion

3.1 BKB Macromonomer

The telechelic macromonomer BKB was successfully synthesized using a Mitsunobu reaction of MeBIP-OH and hydroxyl-terminated poly(ethylene-*co*-butylene) copolymer (M_n = 3,000 g mol^{-1}) (Fig. 2).[18] A titration with the BKB monomer and $Zn(ClO_4)_2$ in $CHCl_3$/ACN was monitored by UV-Vis (Fig. 6). The absorbance of the free MeBIP ligand (319 nm) decreased as the complex of 2 MeBIP ligands (350 nm) with one Zn cation was formed. An isobestic point occurred at a Zn to BKB ratio of 1:1 and confirmed that BKB contains 2 terminal MeBIP ligands per poly(ethylene-*co*-butylene) oligomer chain.

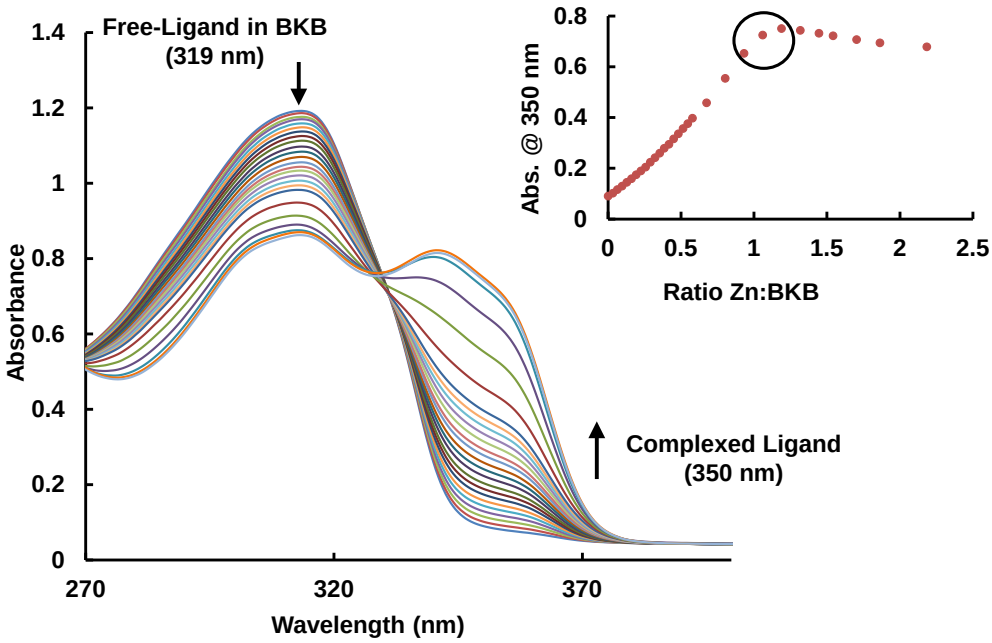

Fig. 6 Titration of BKB with $Zn(ClO_4)_2$ monitored by UV-Vis. Free MeBIP ligand absorbs at 319 nm, and complexed ligand absorbs at 350 nm. As $Zn(ClO_4)_2$ is added, the concentration of free ligand decreases, which results in a decrease in free-ligand absorbance intensity. The concentration of complexed ligand increases, which results an increase in complexed ligand absorbance. At the isobestic point (black circle), the complexed ligand intensity stopped increasing. The inset graph corresponds to the absorbance vs. Zn:BKB ratio during the titration.

3.2 OCT-Functionalized Gold Nanoparticles

Using a homogeneous reaction based on previous work by Peng et al. (Fig. 4),[28] 2-nm OCT-functionalized Au nanoparticles were synthesized. In Fig. 5, the surface plasmon resonance of the OCT-AuNps was measured but not, apparently, in $CHCl_3$. Due to the ultrasmall size of the nanoparticle (<2 nm) and the thiol-capping ligand, the electronics of the nanoparticle core differ from nanoparticles between 5 and 50 nm,[29] and the typical surface plasmon resonance disappears due to the reduction of the number of Au surface atoms to core atoms.[30–32] Bright-field TEM was used to identify the nanoparticle size (Fig. 7) of 1.8 nm. Further investigation into the synthesis of larger Au nanoparticles was successful but with large particle size distribution.

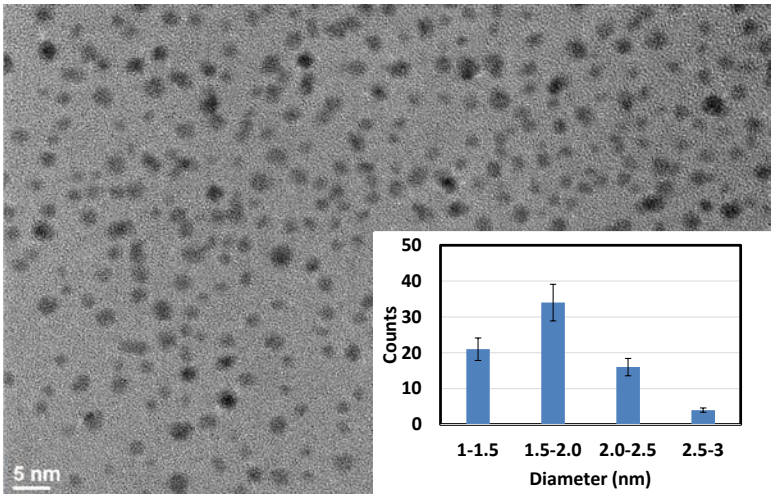

Fig. 7 Bright-field TEM of OCT-AuNps and histogram of nanoparticle sizes

3.3 MeBIP-Functionalized Gold Nanoparticles

Using the adapted conditions optimized for the OCT-AuNps, 2-nm MeBIP-functionalized Au nanoparticles were synthesized. $CHCl_3$ was added to the MeBIP-SH ligand to increase solubility. Equal ratios of OCT to MeBIP-SH were needed to incorporate MeBIP-SH onto the surface of the nanoparticles. Attempts to synthesize 100% MeBIP-SH-capped nanoparticles were unsuccessful, possibly due to the steric and bulky constraints of the MeBIP ligand.[33,34] The OCT helped to separate the MeBIP ligands while still maintaining ligand thiol ligand coverage on the surface of the nanoparticle.[33,34] Ligand exchange experiments with 2-nm OCT-AuNps or 10-nm citric-acid-capped Au nanoparticles with MeBIP-SH were unsuccessful, probably due to the steric constraints with the MeBIP ligand but also due to competing interactions of amine—Au and sulfur—Au atoms. A 1.8-nm nanoparticle size was measured by HAADF STEM (Fig. 8). To measure how many

MeBIP-SH ligands were attached to each Au nanoparticle, a titration of MeBIP-AuNps in $CHCl_3$ with $Zn(ClO_4)_2$ in ACN was monitored by UV-Vis. An isobestic point occurred when 0.06 µmol of Zn^{2+} was added to the solution of MeBIP-AuNps. This corresponds to half of the mols of MeBIP ligand in the sample of nanoparticles. Based on the weight of a 1.8-nm Au nanoparticle and the number of moles of MeBIP per gram measured at the isobestic point of the UV-Vis titration,[33,34] there were 20–30 MeBIP-SH ligands per nanoparticle on average. Estimation of nanoparticle weight was previously explained by Hayes et al.[33,34]

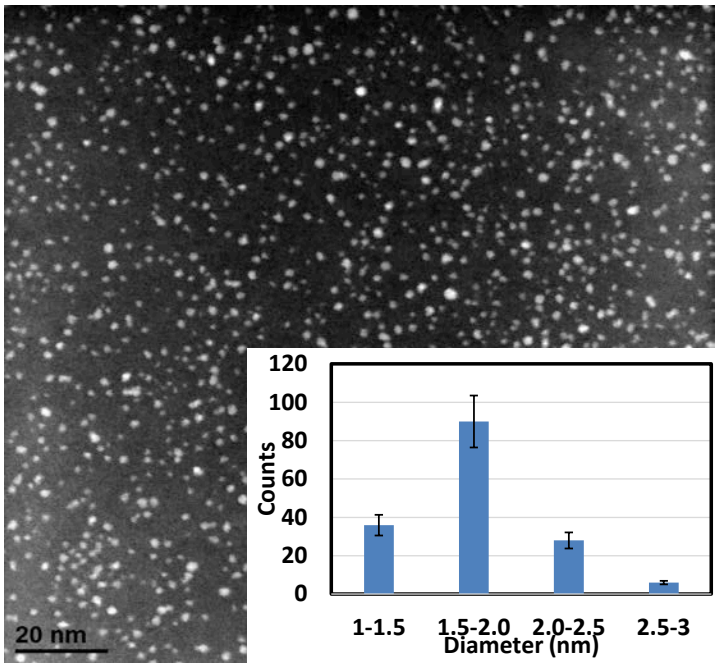

Fig. 8 HAADF STEM of MeBIP-AuNps with inlayed histogram of nanoparticle sizes

3.4 Nanocomposite Films

Both the OCT-AuNps and the MeBIP-AuNps were incorporated into the metallo-supramolecular polymers [BKB:$Zn(ClO_4)_2$], and free-standing films were prepared at several nanoparticle loadings. The OCT-AuNps were loaded into the supramolecular polymers at 0, 1, and 10 wt% to investigate the maximum possible loading. All films were transparent except for the 10-wt% nanocomposite film. MeBIP-AuNps were loaded into the supramolecular polymers at 0.10, 0.15, 0.25, 0.50, 0.60, 1.00, and 1.50 wt%.

The morphology and nanoparticle dispersion of these films were investigated using SAXS and TEM. The scattering peaks at q*, 2q*, 3q*, and 4q* (labeled with black arrows) in Fig. 9 indicated lamellar morphology in the pure BKB:$Zn(ClO_4)_2$ polymer. The peak at 10.67 $Å^{-1}$ corresponded to the distance between metal-ligand complexes previously described.[20] BKB supramolecular polymers typically

exhibited lamellar morphology with divalent metal cations.[18] This microphase-separated morphology stemmed from a hard phase comprising the metal-ligand complexes and a soft phase comprising the poly(ethylene-*co*-butylene) polymer core.[18] For the 1- and 10-wt% OCT-AuNps nanocomposite films, only q*, 2q*, and 3q* Bragg peaks were apparent, with an increase in intensity of the 3q* peak because the OCT-AuNPs disrupt lamellar order. This intensity increase was probably due to increased nanoparticle aggregate scattering. TEM also revealed lamellar morphology in the BKB:$Zn(ClO_4)_2$ film, and this was retained in the 1- and 10-wt% composite films (Fig. 10). However, the 10-wt% nanocomposite film also had a large amount of aggregation and appeared black.

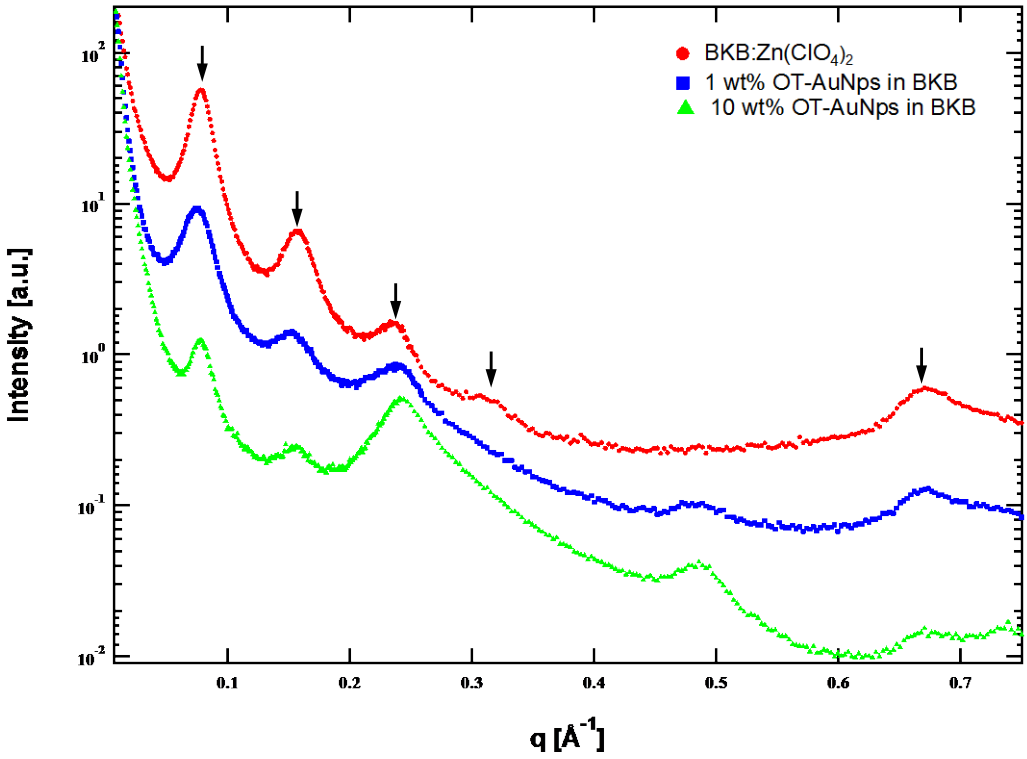

Fig. 9 SAXS of BKB:$Zn(ClO_4)_2$ nanocomposite films

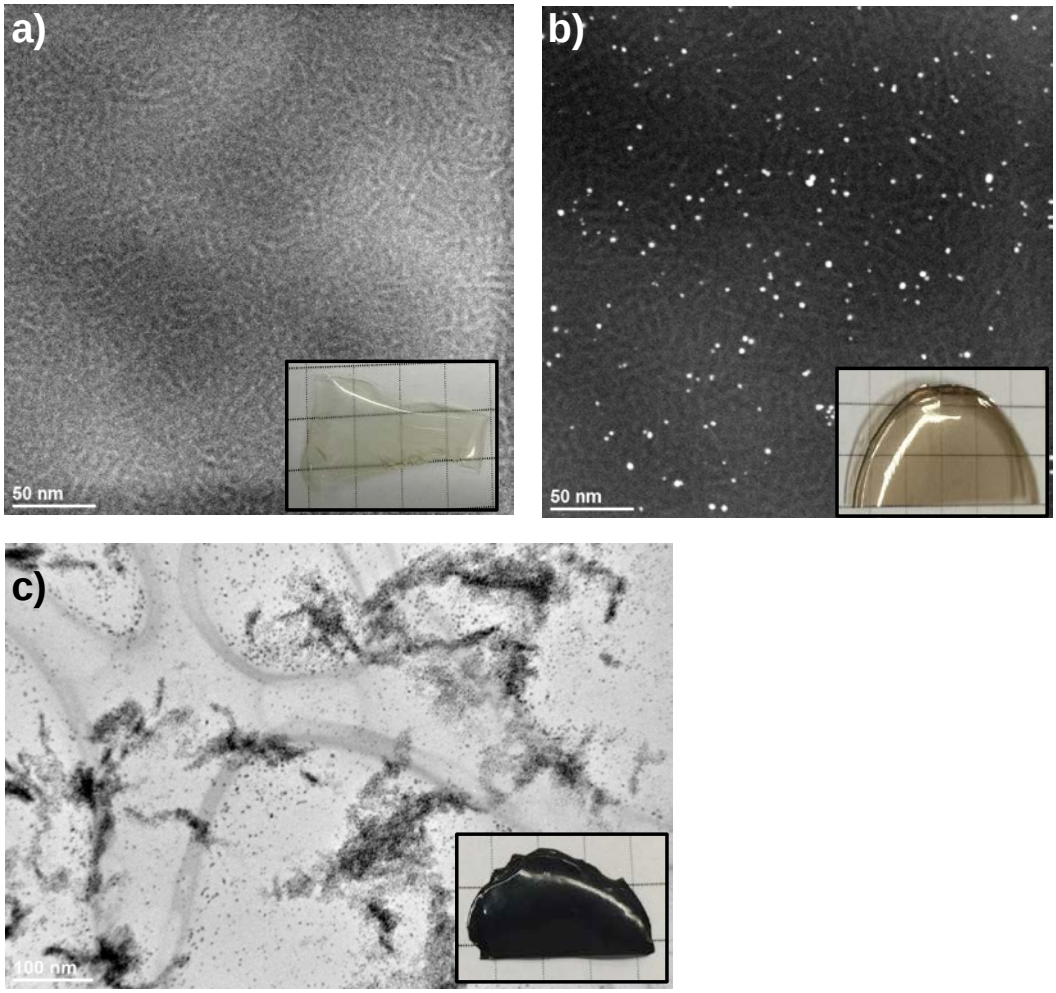

Fig. 10 TEM of OCT-AuNPs nanocomposites: a) pure BKB:$Zn(ClO_4)_2$ supramolecular polymer, b) HAADF STEM of 1-wt% OCT-AuNps nanocomposites, and c) BF TEM of 10-wt% OCT-AuNps on a lace-carbon-coated copper TEM grid

When the MeBIP-AuNps were incorporated into the nanocomposite films, the order of addition during synthesis became crucial. The MeBIP-AuNp solution was added to the BKB solution first, followed by the $Zn(ClO_4)_2$ solution. The SAXS profile does not change significantly between loadings. However, after HAADF STEM experiments it became apparent there was a high level of nanoparticle aggregation even at low nanoparticle loadings (0.15–1.5 wt%) and sonication (Figs. 11b and 11c)

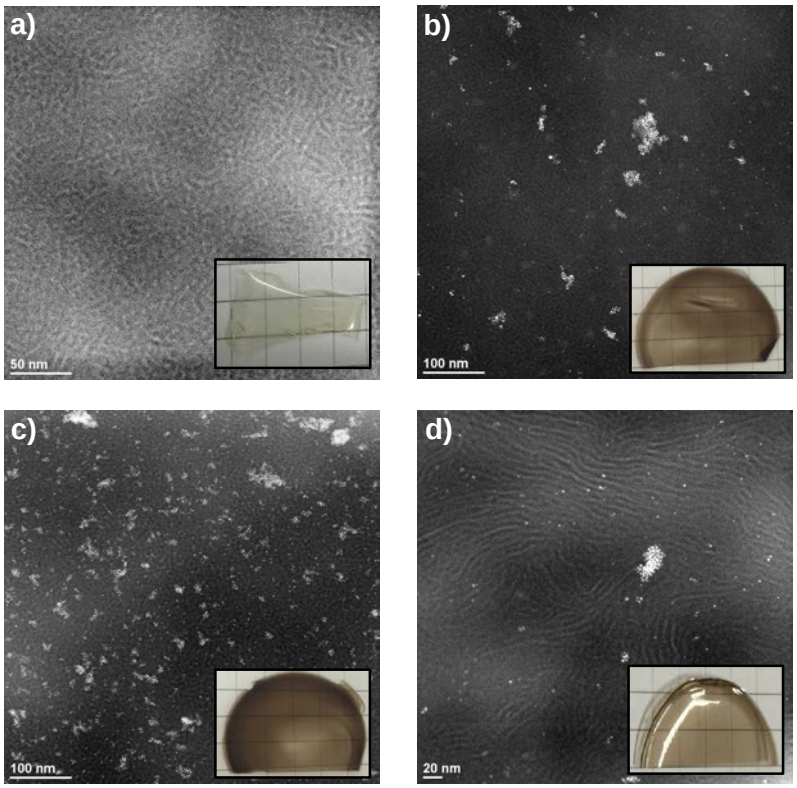

Fig. 11 HAADEF STEM of MeBIP-AuNp nanocomposites: a) pure BKB:$Zn(ClO_4)_2$ supramolecular polymer, b) 0.5% MeBIP-AuNp nanocomposite synthesized from first addition order, c) 1.5% MeBIP-AuNp nanocomposite synthesized from first addition order, and d) 0.25% MeBIP-AuNp nanocomposite synthesized from final addition order

With a change in the order of addition, less nanoparticle aggregation was observed, but macroscopic phase separation occurred in composites containing 0.6 wt% or more. The MeBIP-AuNp solution was added to the $Zn(ClO_4)_2$ solution, followed by the addition of the BKB solution. Interestingly, the supramolecular polymerization gelled upon the addition of the BKB solution and only dissolved upon the addition of more $CHCl_3$.

The morphology of the films prepared using the best sample prep method was investigated with SAXS and TEM. The SAXS profiles of these nanocomposite films were similar to the previous films likely revealing a lamellar morphology (Figs. 12 and 13). HAADF STEM confirmed the lamellar morphology but with more long-range order than the pure BKB:$Zn(ClO_4)_2$ film (Fig. 11d). Possibly, when the $Zn(ClO_4)_2$ is added to the nanoparticle solution, all of the free MeBIP ligand is complexed with a Zn metal cation and ClO_4^- counterion.[35,36] This reduced the amount of aggregation or complexation between nanoparticles and possibly increased the probability of the MeBIP-AuNps from incorporating into the supramolecular polymer assembly.[35,36] The resulting morphology was still lamellar but with increased long-range order.

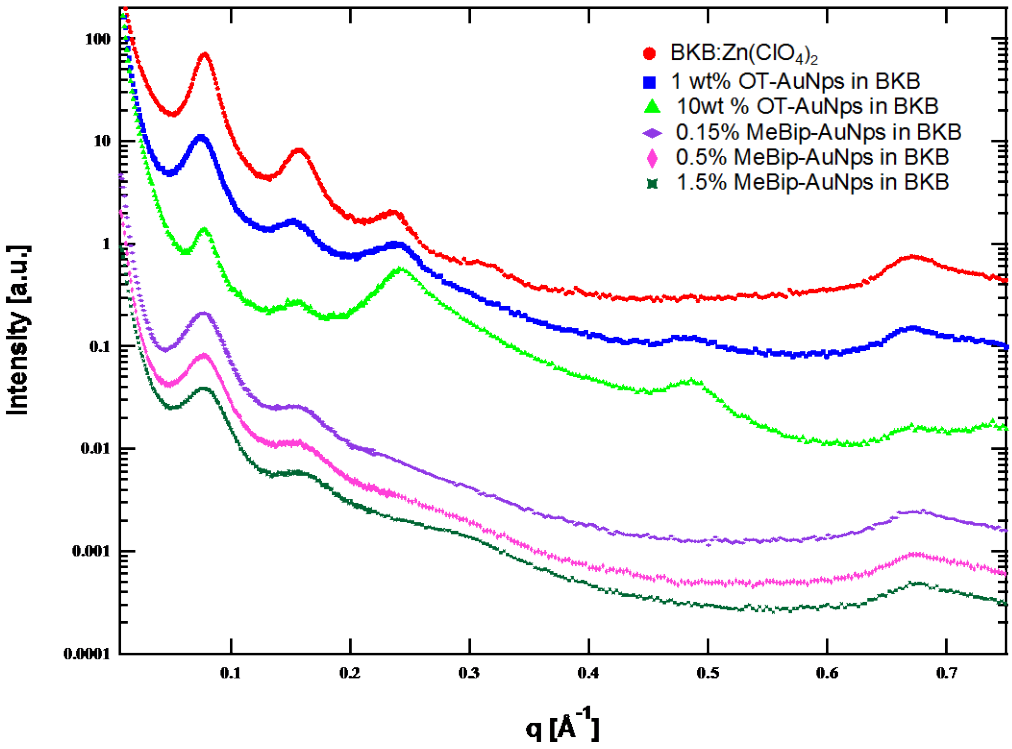

Fig. 12 SAXS of MeBIP-AuNps nanocomposites synthesized in the original addition order

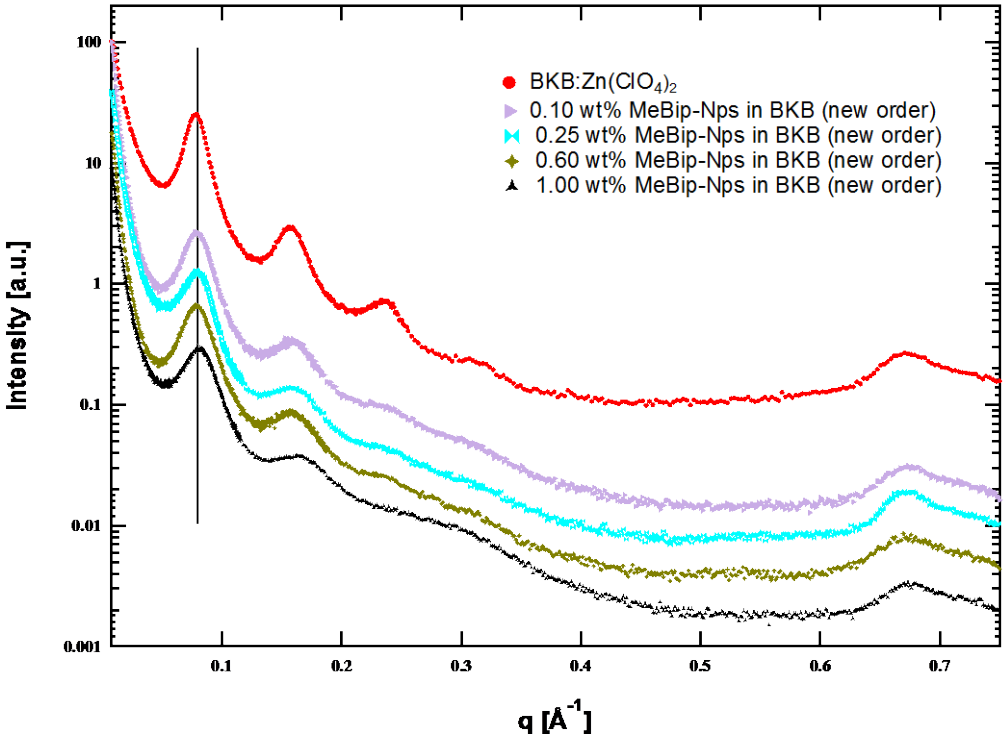

Fig. 13 SAXS of MeBIP-AuNps nanocomposites synthesized in the final addition order

At loadings ≥0.6 wt%, the macrophase aggregation occurred due to nanoparticle precipitation (Fig. 14). At lower loadings, polymer chains deformed to accommodate the functionalized nanoparticles, but this resulted in an entropic penalty. This penalty may become too large with increased nanoparticle concentration, leading to the macrophase separation observed.

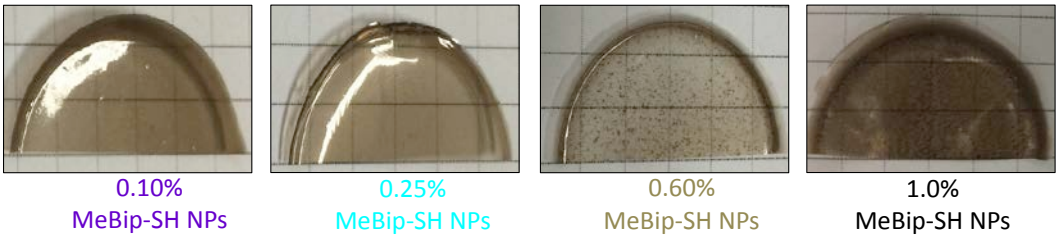

Fig. 14 MeBIP-AuNps nanocomposite films synthesized using the final order of addition

4. Conclusion

The synthesis of MeBIP-functionalized Au nanoparticles was successful, and their incorporation into supramolecular nanocomposites was reported. The morphologies of the nanocomposite films with nanoparticle loadings from 0 to 10 wt% were investigated with SAXS and TEM. The appropriate order of addition during the supramolecular polymer assembly was determined for MeBIP-AuNps-containing nanocomposites and strongly influenced the final morphology of the supramolecular polymer films. Large-scale aggregation and phase separation was detected for MeBIP-AuNps loadings ≥0.6 wt% with lamellar morphology retained for all films.

5. References

1. Kingery, WD, Vandiver P. Ceramic masterpieces: art, structure, and technology. New York (NY): Free Press; 1986.

2. Hussain F, Okamoto M, Gorga RE. Polymer-matrix nanocomposites, processing, manufacturing, and application: an overview. Journal of Composite Materials. 2006;40:1511–1575.

3. Kao J, Thorkelsson K, Bai P, Rancatore BJ, Xu T. Toward functional nanocomposites: taking the best of nanoparticles, polymers, and small molecules. Chemical Society Reviews. 2013;42:2654–2678.

4. Phillips CL, Iacovella CR, Glotzer SC. Stability of the double gyroid phase to nanoparticle polydispersity in polymer-tethered nanosphere systems. Soft Matter. 2010;6:1693–1703.

5. Glotzer SC, Solomon, M. J. Anisotropy of building blocks and their assembly into complex structures. Nature Materials. 2007;6:557–562.

6. Jayaraman A, Schweizer KS. Effective interactions, structure, and phase behavior of lightly tethered nanoparticles in polymer melts. Macromolecules. 2008;41:9430–9438.

7. Puech N, Mora S, Phou T, Porte G, Jestin J, Oberdisse J. Microemulsion nanocomposites: phase diagram, rheology and structure using a combined small angle neutron scattering and reverse Monte Carlo approach. Soft Matter. 2010;6:5605–5614.

8. Fang H-P, Wu Y-H, Lin H-C. Synthesis and study of novel supramolecular nanocomposites containing aryl-imidazo-phenanthroline-based metallo-polymers (H-donors) and surface-modified ZnO nanoparticles (H-acceptors). Tetrahedron. 2013; 69:293–301.

9. Kao J, Bai P, Chuang VP, Jiang Z, Ercius P, Xu T. Nanoparticle assemblies in thin films of supramolecular nanocomposites. Nano Letters. 2012;12:2610–2618.

10. Kao J, Xu T. Nanoparticle assemblies in supramolecular nanocomposite thin films: concentration dependence. Journal of the American Chemical Society. 2015;137:6356–6365.

11. Fox J, Wie JJ, Greenland BW, Burattini S, Hayes W, Colquhoun HM, Mackay ME, Rowan SJ. High-strength, healable, supramolecular polymer nanocomposites. Journal of the American Chemical Society. 2012;134:5362–5368.

12. Zhao Y et al. Small-molecule-directed nanoparticle assembly towards stimuli-responsive nanocomposites. Nature Materials. 2009;8:979–985.

13. De Greef TFA, Smulders MMJ, Wolffs M, Schenning APHJ, Sijbesma RP, Meijer EW. Supramolecular polymerization. Chem Rev. 2009;109:5687–5754.

14. Yang L, Tan X, Wang Z, Zhang X. Supramolecular polymers: historical development, preparation, characterization, and functions. Chemical Reviews. 2015;115:7196–7239.

15. Brunsveld L, Folmer JB, Meijer EW, Sijbesma RP. Supramolecular polymers. Chemical Reviews. 2001;101:4071–4097.

16. Fox JD, Rowan SJ. Supramolecular polymerizations and main-chain supramolecular polymers. Macromolecules. 2009;42:6823–6835.

17. Wojtecki RJ, Meador MA, Rowan SJ. Using the dynamic bond to access macroscopically responsive structurally dynamic polymers. Nature Materials. 2011;10:14–27.

18. Burnworth M, Tang L, Kumpfer JR, Duncan AJ, Beyer FL, Fiore GL, Rowan SJ, Weder C. Optically healable supramolecular polymers. Nature. 2011;472:334–337.

19. Rowan SJ, Beck JB. Metal–ligand induced supramolecular polymerization: a route to responsive materials. Faraday Discussions. 2005;128:43–53.

20. Kumpfer JR, Jin J, Rowan SJ. Stimuli-responsive europium-containing metallo-supramolecular polymers. Journal of Materials Chemistry. 2010;20:145–151.

21. Sivakova S, Bohnsack DA, Mackay ME, Suwanmala P, Rowan SJ. Utilization of a combination of weak hydrogen-bonding interactions and phase segregation to yield highly thermosensitive supramolecular polymers. Journal of the American Chemical Society. 2005;127:18202–18211.

22. Kumpfer JR, Rowan SJ. Stimuli-responsive europium-containing metallo-supramolecular polymers. Journal of the American Chemical Society. 2011;133:12866–12874.

23. Beck JB, Ineman JM, Rowan SJ. Metal/ligand-induced formation of metallo-supramolecular polymers. Macromolecules. 2005;38:5060–5068.

24. Kumpfer JR, Wie JJ, Swanson JP, Beyer FL, Mackay ME, Rowan SJ. Influence of metal ion and polymer core on the melt rheology of metallosupramolecular films. Macromolecules. 2012;45:473–480.

25. Hsu WY, Gierke TD, Molnar C J. Morphological effects on the physical properties of polymer composites. Macromolecules. 1983;16:1945–1947.

26. Zhang F, Ilavsky J, Long GG, Quintana JPG, Allen AJ, Jemian PR. Glassy carbon as an absolute intensity calibration standard for small-angle scattering. Metallurgical and Materials Transactions A. 2009;41:1151–1158.

27. Ilavsky J, Jemian PR. Irena: tool suite for modeling and analysis of small-angle scattering. Journal of Applied Crystallography. 2009;42:347–353.

28. Jana NR, Peng X. Single-phase and gram-scale routes toward nearly monodisperse Au and other noble metal nanocrystals. Journal of the American Chemical Society. 2003;125:14280–14281.

29. Kim BH, Hackett MJ, Park J, Hyeon T. Synthesis, characterization, and application of ultrasmall nanoparticles. Chemistry of Materials. 2014;26:59–71.

30. Crespo P, Litran R, Rojas TC, Multigner M, de la Fuente JM, Sanchez-Lopez JC, Garcia MA, Hernando A, Penades S, Fernandez A. Permanent magnetism, magnetic anisotropy, and hysteresis of thiol-capped gold nanoparticles. Physical Review Letters. 2004;93:087204.

31. Meng X, Liu Z, Zhu M, Jin R. Controlled reduction for size selective synthesis of thiolate protected gold nanoclusters Aun (n = 20, 24, 39, 40). Nanoscale Research Letters. 2012;7:1–7.

32. Suda M, Kameyama N, Suzuki M, Kawamura N, Einaga Y. Reversible phototuning of ferromagnetism at Au-S interfaces at room temperature. Angewandte Chemie. 2008:47:160–163.

33. Vaiyapuri R, Greenland BW, Colquhoun HM, Elliott JM, Hayes W. Molecular recognition between functionalized gold nanoparticles and healable, supramolecular polymer blends – a route to property enhancement. Polymer Chemistry. 2013;4:49020–4909.

34. Vaiyapuri R, Greenland BW, Rowan SJ, Colquhoun HM, Elliott JM, Hayes W. Thermoresponsive supramolecular polymer network comprising

pyrene-functionalized gold nanoparticles and a chain-folding polydiimide. Macromolecules. 2012;45:5567–5574.

35. Montalti M, Prodi, L, Zaccheroni N, Beltrame M, Morotti T, Quici S. Stabilization of terpyridine covered gold nanoparticles by metal ions complexation. New Journal of Chemistry. 2007;31:102–108.

36. Norsten TB, Frankamp BL, Rotello VM. Metal directed assembly of terpyridine-functionalized gold nanoparticles. Nano Letters. 2002;2:1345–1348.

List of Symbols, Abbreviations, and Acronyms

ACN	acetonitrile
ANL	Argonne National Laboratory
Au	gold
AuNp	gold nanoparticle
$AuCl_3$	gold chloride
BKB	telechelic macromonomer
$CHCl_3$	chloroform
DDAB	didodecyldimethylammonium bromide
DMF	*N*,*N*-dimethylformamide
DMSO	dimethyl sulfoxide
HAADF STEM	high-angle annular dark field scanning transmission electron microscopy
HCl	hydrochloric acid
KOH	potassium hydroxide
MeBIP	2,6-bis(1'-methyl-benzimidazolyl)-4-hydroxypyridine
MeBIP-SH	2,6-bis(1'-methyl-benzimidazoyl)-4-(12-thiododecyl) pyridine
MeOH	methanol
NIR	near-infrared
OCT	1-octanethiol
SAXS	small-angle X-ray scattering
TBAB	borane tert-butylamine complex
TEM	transmission electron microscopy
UV-Vis	ultraviolet-visible
$Zn(ClO_4)_2$	zinc (II) perchlorate hexahydrate

1 (PDF) DEFENSE TECHNICAL INFORMATION CTR DTIC OCA

2 (PDF) DIRECTOR US ARMY RESEARCH LAB RDRL CIO LL IMAL HRA MAIL & RECORDS MGMT

1 (PDF) GOVT PRINTG OFC A MALHOTRA

3 (PDF) DIR USARL RDRL WMM G A SAVAGE R LAMBETH F BEYER